### **MATERIALS SCIENCE**

# Atomistic mechanisms of water vapor-induced surface passivation

Xiaobo Chen<sup>1</sup>, Weitao Shan<sup>2</sup>, Dongxiang Wu<sup>1</sup>, Shyam Bharatkumar Patel<sup>1</sup>, Na Cai<sup>1</sup>, Chaoran Li<sup>1</sup>, Shuonan Ye<sup>1</sup>, Zhao Liu<sup>3</sup>, Sooyeon Hwang<sup>4</sup>, Dmitri N. Zakharov<sup>4</sup>, Jorge Anibal Boscoboinik<sup>4</sup>, Guofeng Wang<sup>2</sup>, Guangwen Zhou<sup>1</sup>\*

The microscopic mechanisms underpinning the spontaneous surface passivation of metals from ubiquitous water have remained largely elusive. Here, using in situ environmental electron microscopy to atomically monitor the reaction dynamics between aluminum surfaces and water vapor, we provide direct experimental evidence that the surface passivation results in a bilayer oxide film consisting of a crystalline-like  $Al(OH)_3$  top layer and an inner layer of amorphous  $Al_2O_3$ . The  $Al(OH)_3$  layer maintains a constant thickness of ~5.0 Å, while the inner  $Al_2O_3$  layer grows at the  $Al_2O_3$ /Al interface to a limiting thickness. On the basis of experimental data and atomistic modeling, we show the tunability of the dissociation pathways of  $H_2O$  molecules with the  $Al_2O_3$ , and  $Al(OH)_3$  surface terminations. The fundamental insights may have practical significance for the design of materials and reactions for two seemingly disparate but fundamentally related disciplines of surface passivation and catalytic  $H_2$  production from water.



Commons Attribution

License 4.0 (CC BY).

### INTRODUCTION

The interaction of water with solid surfaces is central to many surface chemical processes such as geochemistry, corrosion, catalysis, and electrochemistry (1-5). Many studies exist that detail the behavior of water across small lengths and time scales by carefully dosing small amounts of water onto a solid surface at cryogenic temperatures (6, 7). While this approach has been successful in revealing the structure properties within the adlayer of condensed water, the resulting understanding obtained under such rarefied conditions does not translate into an equally good understanding of surface phenomena occurring in technologically relevant conditions, where the chemical reactions between adsorbed water and the solid become highly relevant. The development of aberration-corrected environmental transmission electron microscopy (ETEM) opens a unique window of atomically understanding gas-surface reactions under realistic conditions of pressure and temperature. This is exemplified by the ETEM observations of the various surface oxidation phenomena of aluminum (Al) in dry O2, showing the liquid-like self-healing of the amorphous Al oxide film to match the deformation of the Al substrate (8), crystal orientation-dependent Al oxide film nucleation and growth (9), and a two-stage oxidation process starting from intralayer atomic disordering to interlayer disordering leading to the formation of an amorphous Al oxide layer (10).

Here, we use ETEM to directly probe water vapor—induced oxide film growth on Al surfaces. Specifically, we illustrate how water vapor induces dynamic transformations of the metal lattice into its oxides at room temperature, which has not been attained yet at the atomic scale but is practically important because of the wide use of Al for applications where corrosion resistance is required (8, 11– 15). On the basis of directly observed Al(OH)<sub>3</sub>/Al<sub>2</sub>O<sub>3</sub> bilayer film growth consisting of an upper layer of crystalline-like Al(OH)<sub>3</sub> and an inner layer of amorphous Al<sub>2</sub>O<sub>3</sub> on Al surfaces in water vapor, this work demonstrates the tunability of the H<sub>2</sub>O dissociation pathway at the ambient temperature. That is, H<sub>2</sub>O molecules dissociate into OH and H on pristine Al and amorphous Al<sub>2</sub>O<sub>3</sub> to result in the surface hydrolysis into Al(OH)<sub>3</sub>. The Al(OH)<sub>3</sub> layer facilitates the dissociation of H<sub>2</sub>O molecules into H<sub>2</sub> molecules due to the inward O diffusion for the Al<sub>2</sub>O<sub>3</sub> interfacial growth to a limiting thickness. These results not only offer the microscopic mechanism underlying the onset of a surface passivation process and its subsequent progression toward the self-limiting regime but also demonstrate the tunability of the dissociation pathways of H<sub>2</sub>O molecules with the hydroxylation of Al surfaces. These fundamental insights may have practical implications, related not only to the microscopic processes of the passivating film growth but also to catalytic H<sub>2</sub> production from H<sub>2</sub>O over the spontaneously formed Al hydroxide overlayer on Al.

### **RESULTS**

# $Al(OH)_3/Al_2O_3$ bilayer film growth on Al surfaces in $H_2O$ vapor

Figure 1 illustrates in situ high-resolution TEM (HRTEM) images, in cross-sectional view along the  $[1\overline{10}]$  zone axis, revealing the dynamic transformation of Al lattice into Al oxides while exposing a clean Al(111) surface at 298 K to  $3.5\times10^{-5}$  torr of water vapor. As seen in Fig. 1A, the interplanar spacing of 2.3 Å corresponds to the Al(111) planes (more details in the sections "Sample preparation" and "In situ HRTEM experiments and fig. S1). The shape of the atom columns in the topmost layer surface shows some elongation along the (200) lattice planes, which may originate from the lattice damage induced by the condensed electron beam bombardment inside the TEM to sputter off air-formed native oxide. Because

<sup>&</sup>lt;sup>1</sup>Materials Science and Engineering Program and Department of Mechanical Engineering, State University of New York at Binghamton, Binghamton, NY 13902, USA. <sup>2</sup>Department of Mechanical Engineering and Materials Science, University of Pittsburgh, Pittsburgh, PA 15261, USA. <sup>3</sup>Department of Electrical and Computer Engineering, State University of New York at Binghamton, Binghamton, NY 13902, USA. <sup>4</sup>Center for Functional Nanomaterials, Brookhaven National Laboratory, Upton, NY 11973, USA.

<sup>\*</sup>Corresponding author. Email: gzhou@binghamton.edu

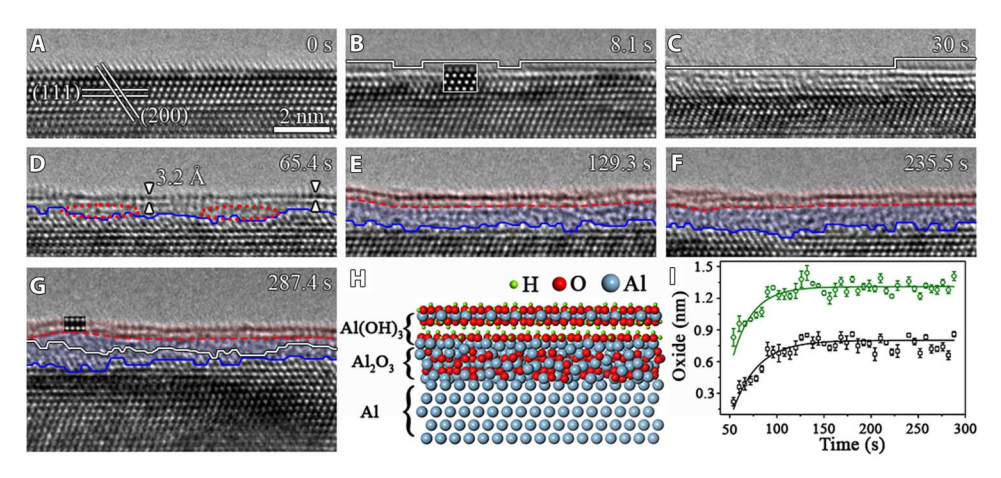


Fig. 1. Water vapor–induced surface passivation of pristine Al(111). (A to G) Time-sequence high-resolution TEM (HRTEM) images (movie S1) showing the Al(OH) $_3$ /Al $_2$ O $_3$  bilayer film growth at 298 K in pH $_2$ O  $\approx 3.5 \times 10^{-5}$  torr. The solid white lines highlight the weakened lattice contrast regions owing to the H $_2$ O adsorption–induced extraction of Al atoms from the outermost surface layer of pristine Al(111). The dashed red lines and solid blue lines mark the Al(OH) $_3$ /Al $_2$ O $_3$  and Al $_2$ O $_3$ /Al(111) interfaces, respectively. The solid white line in (G) is the superimposed trace of the position and profile of the Al $_2$ O $_3$ /Al(111) interface at t = 65.4 s in (D). The insets in (B) and (G) are simulated HRTEM images based on the Al lattice with atomic vacancies in the topmost layer and the Al(OH) $_3$  structure, respectively. (H) Schematic atomic view of the Al (OH) $_3$ /Al $_2$ O $_3$  bilayer structure. (I) Time dependence of the Al(OH) $_3$ /Al $_2$ O $_3$  bilayer film thickness (green) and the Al $_2$ O $_3$ /Al(111) interface displacement distance (black), where the average thickness of the oxide across the whole surface (within the field of view) is measured at ~60 s of the H $_2$ O dosing, after which the surface is fully covered by the Al(OH) $_3$  layer that stays at a constant thickness of ~5.0 Å, while the inner amorphous Al $_2$ O $_3$  layer grows to a limiting thickness. The error bars represent SD uncertainties based on multiple measurements on the in situ TEM images.

the native oxide on Al is amorphous, the continuation of the crystal lattice planes along the (200) lattice plane to the topmost layer suggests that the as-prepared Al(111) surface is largely oxide-free. Upon the H<sub>2</sub>O exposure, some areas of the outermost layer show weakened image contrast (marked by solid white lines in Fig. 1 (B and C) due to the formation of atomic vacancies in the topmost layer, as shown by the simulated HRTEM image (Fig. 1B, inset). This indicates the extraction of Al atoms from the topmost layer as a result of the large reaction exothermicity of dissociative adsorption of H<sub>2</sub>O molecules. This is also consistent with many surface science experiments and the prediction from atomistic simulations, showing that the dissociative adsorption of gas molecules on metallic surfaces typically results in one-atomic layer-deep pits and adatoms extracted from the surface (16-21). The exfoliation of the outermost Al results in the hydroxylation of the two inner atomic layers, which leads to the expansion of the interplanar spacing from 2.3 Å of the pristine Al(111) lattice (Fig. 1A) to ~3.2 Å (distance between the center of the atom columns in the two topmost layers) in the region highlighted by the triangular markers in Fig. 1D, the latter of which matches well the interplanar spacing of Al(OH)<sub>3</sub>(112) planes (22–24).

Continued  $H_2O$  exposure results in the attack toward deeper atomic layers of the Al substrate, as shown by the loss of lattice contrast in local regions marked with dashed red circles in Fig. 1D. Upon further  $H_2O$  exposure, the crystalline Al lattice in the subsurface region gradually transforms into amorphous,  $Al_2O_3$ -like oxide, as seen from the time-sequence images in Fig. 1 (E to G). By contrast, the  $Al(OH)_3$  overlayer maintains the crystalline state with clearly visible image contrast of individual atom columns, as further evidenced by the inset HRTEM simulation image. The in situ TEM observation indicates that the  $H_2O$  exposure results in the  $Al(OH)_3/Al_2O_3$  bilayer film growth, which is also cross-validated by x-ray photoelectron spectroscopy (XPS) measurements of the surface chemistry shown later. The  $Al_2O_3/Al(111)$  interface is

atomically rough and displays an overall inward movement toward the Al side. This is evident from the detailed tracing of the movement of the Al<sub>2</sub>O<sub>3</sub>/Al(111) interface depicted in Fig. 1G, where the relative positions of the interface at 65.4 and 287.4 s are given for comparison and show that the interface moves toward the metal side by ~3.5± 0.5 Å within an elapsed time of 222 s. By contrast, the upper Al(OH)<sub>3</sub> layer maintains a constant thickness of  $\sim 5.0$  Å [the distance between the outermost edge of the atom columns in the topmost layer and the Al<sub>2</sub>O<sub>3</sub>/Al(111) interface], while the inner Al<sub>2</sub>O<sub>3</sub> layer thickens by inward migration of the atomically rough  $Al_2O_3/Al(111)$  interface. This indicates that  $H_2O$  molecules on the pristine Al(111) dissociate dominantly into OH<sup>-</sup> and H<sup>+</sup> to result in the formation of the Al(OH)<sub>3</sub> layer. Thereafter, the observed inward Al<sub>2</sub>O<sub>3</sub> film growth is induced by the inward diffusion of O atoms derived from the dissociative H<sub>2</sub>O adsorption on the Al(OH)<sub>3</sub> overlayer. The randomly arriving O atoms at the Al<sub>2</sub>O<sub>3</sub>/Al(111) interface are incorporated into the Al lattice at any site of the interface (10, 25), thereby resulting in the atomically rough  $Al_2O_3/Al(111)$ interface morphology. The schematic atomic structure of the Al (OH)<sub>3</sub>/Al<sub>2</sub>O<sub>3</sub> bilayer configuration is illustrated in Fig. 1H.

Figure 1I shows the measurement of the thickness evolution of the  $Al(OH)_3/Al_2O_3$  bilayer film and the inward displacement distance of the  $Al_2O_3/Al(111)$  interface over the course of time, both of which display an initial fast growth followed by notably slower thickening to a limiting-thickness regime. This self-limiting growth behavior can be fitted well with the logarithmic growth law of the Cabrera-Mott model (Fig. 1I), where the difference between the two self-limiting growth curves differs by ~5.0 Å that corresponds to the thickness of the upper  $Al(OH)_3$  layer that stays constant with time once formed. As stipulated by the Cabrera-Mott theory, the self-limiting oxide film growth results from electron tunneling from the metal through the oxide film to adsorbed O that leads to a self-generated electric field across the oxide film, which lowers the energy barrier for ion migration across the oxide film

and makes the oxide film growth possible at a low temperature (where the thermally driven diffusion is negligible) (26). Because the tunneling current decreases exponentially with increasing the thickness of the oxide film, the oxidation stops at a limiting thickness of the oxide film. The magnitude of the self-generated electric field depends on the surface coverage of O (or OH derived from dissociative  $\rm H_2O$  adsorption) to accept the tunneling electrons, where a higher O (or OH) coverage corresponds to a stronger electric field and thus a larger limiting thickness (27–29). This is consistent with our ex situ TEM observations, showing a larger limiting thickness (~5.7 nm) of the  $\rm Al(OH)_3/Al_2O_3$  bilayer oxide film formed in deionized (DI) water.

Figure 2 presents time-sequenced HRTEM images illustrating the evolution of the Al(100) surface viewed along the [001] zone axis, in the course of the  $H_2O$  exposure at  $8.5 \times 10^{-5}$  torr and 298 K. The freshly produced Al(100) surface is atomically flat, and the interplanar spacing (~2.0 Å) matches well the interplanar spacing of Al(200) planes (Fig. 2A). The H<sub>2</sub>O exposure results in the extraction of Al atoms from the topmost layer, as indicated by the weakened lattice contrast in the region marked by the solid white line in Fig. 2B and simulated HRTEM image (Fig. 2B, inset). Upon the continued H<sub>2</sub>O exposure, more Al atoms are extracted from the topmost layer, thereby resulting in the formation of a monolayerdeep depression (pit) and hydroxylation of the two atomic planes at the bottom of the depression, as indicated by the increased interplanar spacing from 2.0 Å of the pristine Al(100) lattice to 2.9 Å in the region marked by the white triangles in Fig. 2C. Meanwhile, Fig. 2C also shows that the surface region adjacent to the depression undergoes the lattice spacing expansion to 2.9 Å, indicating its direct hydroxylation without abstracting Al atoms from that surface region. This surface pitting process transforms the initially atomically flat surface into an uneven morphology of the hydroxylated surface, as shown in Fig. 2 (D to H). Similar to the Al(111) surface, the hydroxylation reaction on the Al(100) surface from

the longer H<sub>2</sub>O exposure also results in Al(OH)<sub>3</sub>/Al<sub>2</sub>O<sub>3</sub> bilayer film growth, and the top Al(OH)<sub>3</sub> layer maintains its crystalline state and the constant thickness (~5.0 Å), while the inner amorphous Al<sub>2</sub>O<sub>3</sub> layer grows to a limiting thickness via the inward movement of the Al<sub>2</sub>O<sub>3</sub>/Al(100) interface. Figure 2I shows the thickness evolution of the Al(OH)<sub>3</sub>/Al<sub>2</sub>O<sub>3</sub> bilayer film and the inward displacement distance of the Al<sub>2</sub>O<sub>3</sub>/Al(100) interface, both of which display a self-limiting growth behavior and can be fitted well with the logarithmic growth law of the Cabrera-Mott model. In contrast to the Al<sub>2</sub>O<sub>3</sub>/Al(111) interface that remains atomically rough during the Al<sub>2</sub>O<sub>3</sub> growth (Fig. 1), the Al<sub>2</sub>O<sub>3</sub>/Al(100) interface consists of flat (100) terraces and monoatomic ledges. Our in situ TEM observation shows that the interfacial Al<sub>2</sub>O<sub>3</sub> growth occurs via lateral flow of ledges along the interface, and these ledges are supplied by repeated nucleation at the Al<sub>2</sub>O<sub>3</sub>/Al(100) interface through interface O embedment into the Al lattice (Fig. 2 (E to H).

Figure 3 presents real-time HRTEM images displaying the hydroxylation reaction of an intersection region between flat (100) and a highly stepped facet exposed to  $3.5 \times 10^{-4}$  torr of H<sub>2</sub>O vapor at 298 K. The H<sub>2</sub>O adsorption results in the abstraction of Al atoms from the outermost layer of the (100) facet, as indicated by the weakened image contrast marked by the solid white lines in Fig. 3 (B and C). This is accompanied by the surface hydroxylation of the topmost two atomic layers, as indicated by the lattice expansion from 2.0 Å of the pristine Al(100) lattice to 2.9 Å. By contrast, the adjacent stepped facet does not show obvious Al abstraction from the topmost surface layer. Instead, the H<sub>2</sub>O adsorption leads to the disordering of the two topmost two atomic layers (the region marked by the dashed white rectangle in Fig. 3B), followed by their transition to the crystalline Al(OH)<sub>3</sub>, as indicated by the restored lattice contrast in the region marked by the dashed white rectangle in Fig. 3C (see more example in fig. S2). Upon continued H<sub>2</sub>O exposure, the formation of amorphous Al<sub>2</sub>O<sub>3</sub> occurs underneath the Al(OH)<sub>3</sub> overlayer that remains a constant thickness

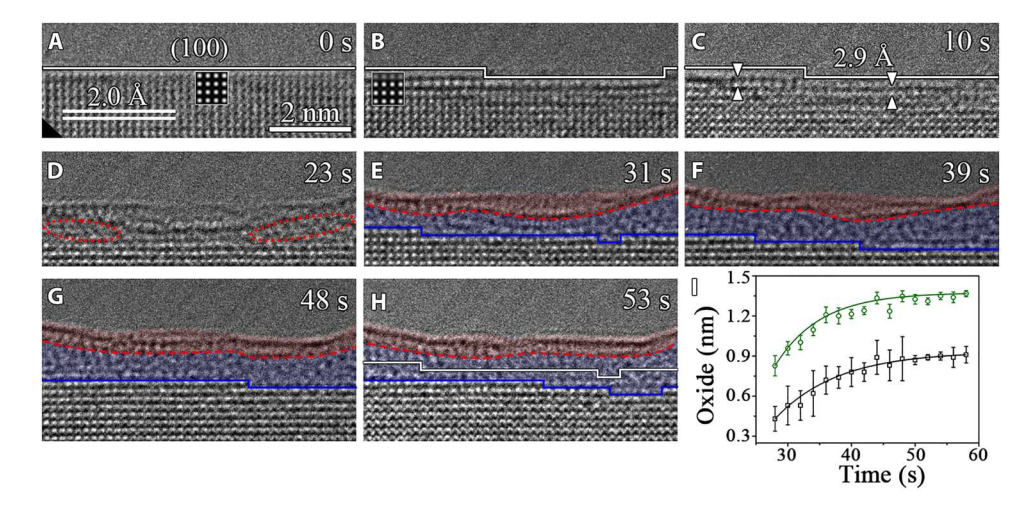


Fig. 2. Water vapor–induced surface passivation of pristine Al(100). (A to H) Time-sequence HRTEM images (movie S2 captured by a direct detection camera) showing the Al(OH) $_3$ /Al $_2$ O $_3$  bilayer film growth at 298 K in pH $_2$ O  $\approx 8.5 \times 10^{-5}$  torr. The regions marked by solid white lines show weakened image contrast-induced by the extraction of Al atoms from outermost layer upon the surface adsorption of H $_2$ O molecules. The insets in (A) and (B) are simulated HRTEM images of the perfect Al lattice and the Al lattice with atomic vacancies in the topmost layer. The dashed red and solid blue lines outline the Al(OH) $_3$ /Al $_2$ O $_3$  and Al $_2$ O $_3$ /Al(100) interfaces, respectively. The solid white line in (H) is the superimposed trace of the position and profile of the Al $_2$ O $_3$ /Al(100) interface at t = 31 s in (E). (I) Time evolution of the Al(OH) $_3$ /Al $_2$ O $_3$  bilayer film thickness (green) and the Al $_2$ O $_3$ /Al(100) interface displacement distance (black), where the error bars represent SD uncertainties based on multiple measurements on the in situ TEM images.

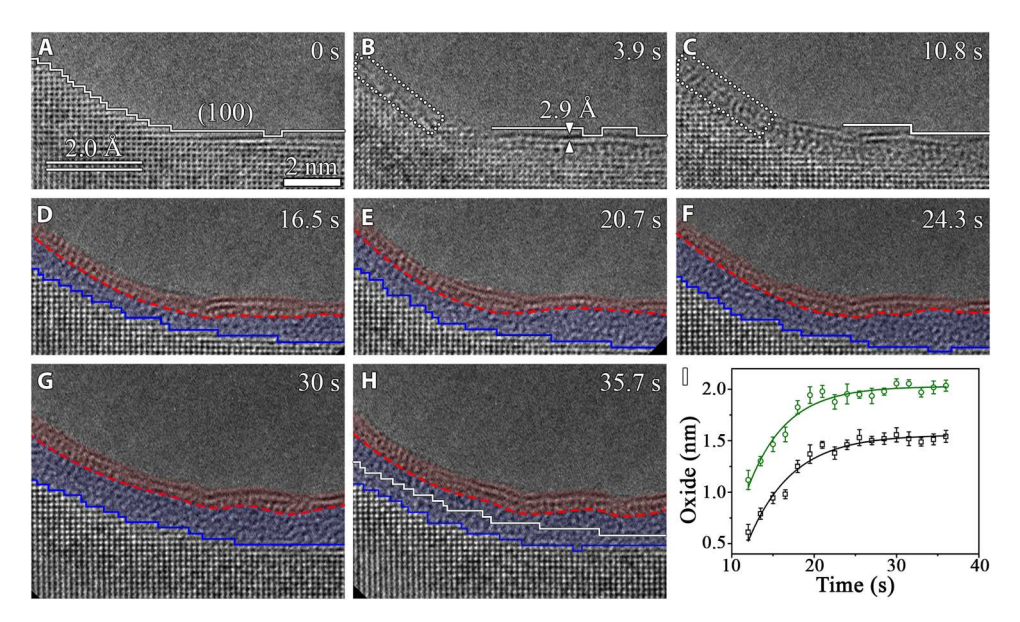


Fig. 3. Water vapor–induced surface passivation of a corner region consisting of a flat (100) facet and a stepped facet. (A to H) Time-sequence HRTEM images (movie S3) showing the Al(OH)<sub>3</sub>/Al<sub>2</sub>O<sub>3</sub> bilayer film growth at 298 K in pH<sub>2</sub>O  $\approx 3.5 \times 10^{-4}$  torr. The dashed white rectangles mark the H<sub>2</sub>O adsorption–induced direct disordering of the stepped facet before its Al(OH)<sub>3</sub> outer layer is established. The dashed red and solid blue lines mark the Al(OH)<sub>3</sub>/Al<sub>2</sub>O<sub>3</sub> and Al<sub>2</sub>O<sub>3</sub>/Al interfaces, respectively. The solid white line in (H) is the superimposed trace of the position and profile of the Al<sub>2</sub>O<sub>3</sub>/Al interface at t = 16.5 s in (D). Scale bar, 2 nm (A to H). (I) Time evolution of the Al(OH)<sub>3</sub>/Al<sub>2</sub>O<sub>3</sub> bilayer film thickness (green) and the Al<sub>2</sub>O<sub>3</sub>/Al interface displacement distance (black), where the error bars represent SD uncertainties based on multiple measurements on the in situ TEM images.

and stays adherent to the  $Al_2O_3$  layer despite the uneven surface morphology (Fig. 3, D to H). The  $Al_2O_3$  layer thickens via the oxide growth at the  $Al_2O_3/Al$  interface, where the (100) interface growth occurs via the nucleation and lateral flow of interfacial ledges, whereas the adjacent stepped interface maintains atomically rough during the  $Al_2O_3$  growth, as indicated by the blue lines in Fig. 3 (D to H). Similar to the (111) and (100) surfaces, both the thickness evolution of the  $Al(OH)_3/Al_2O_3$  bilayer and the  $Al_2O_3/Al$  interface displacement distance can be fitted well with the logarithmic growth law of the Cabrera-Mott model, as shown in Fig. 3I.

# H<sub>2</sub>O vapor-induced Al(OH)<sub>3</sub> formation on amorphous Al<sub>2</sub>O<sub>3</sub>

The in situ TEM observations shown above demonstrate that the H<sub>2</sub>O exposure results in the Al(OH)<sub>3</sub>/Al<sub>2</sub>O<sub>3</sub> bilayer oxide growth on the Al surfaces. The Al(OH)<sub>3</sub> overlayer maintains a crystalline state at a constant thickness, while the underlying amorphous Al<sub>2</sub>O<sub>3</sub> layer grows inward at the Al<sub>2</sub>O<sub>3</sub>/Al interface. Figure 4 shows in situ TEM observations that further confirm this inherent feature of forming a crystalline Al(OH)<sub>3</sub> overlayer from the H<sub>2</sub>Oinduced surface hydroxylation at 298 K. As shown in Fig. 4A, the Al(OH)<sub>3</sub>/Al<sub>2</sub>O<sub>3</sub> bilayer is visible from the H<sub>2</sub>O exposure onto a clean Al(111) surface, where the Al(OH)<sub>3</sub>/Al<sub>2</sub>O<sub>3</sub> and Al<sub>2</sub>O<sub>3</sub>/Al interfaces are indicated by the dashed red and solid blue lines, respectively. The crystalline Al(OH)<sub>3</sub> overlayer can be purposely sputtered off inside the TEM with a condensed electron beam  $> \sim 60,000 e \text{ Å}^{-2}$  $s^{-1}$  (in the presence of  $H_2O$  vapor), leaving behind largely the amorphous Al<sub>2</sub>O<sub>3</sub> layer with a thinner thickness, as illustrated in Fig. 4B. Soon after the electron beam is spread, the crystalline feature starts to rebuild locally on the amorphous Al<sub>2</sub>O<sub>3</sub> layer, such as in the region marked by the dashed red line in Fig. 4C. This trend becomes more evident, and the outermost amorphous region of the entire surface gradually transforms into the crystalline state of  $Al(OH)_3$ . This resumes the  $Al(OH)_3/Al_2O_3$  bilayer configuration, in which the inner  $Al_2O_3$  layer still maintains the amorphous state. The recovered  $Al(OH)_3$  layer also demonstrates the dissociation of  $H_2O$  molecules on the amorphous  $Al_2O_3$  into OH and H to result in the formation of the  $Al(OH)_3$  outer layer. This is indicated by the increased overall thickness of the  $Al(OH)_3/Al_2O_3$  bilayer film via the inward  $Al_2O_3$  growth along the atomically rough  $Al_2O_3/Al(111)$  interface, as shown by tracing the movement of the  $Al_2O_3/Al(111)$  interface depicted in Fig. 4F.

The above in situ TEM results of the Al(OH)<sub>3</sub>/Al<sub>2</sub>O<sub>3</sub> bilayer film growth are confirmed from various experiments conducted on different regions of multiple samples (figs. S2 to S5). When working with in situ TEM observations (Figs. 1 to 4 and fig. S2), the electron beam effects such as radiolysis and local heating need to be carefully examined. It was reported that a strong electron flux  $> \sim 12,000 e$ Å<sup>-2</sup> s<sup>-1</sup> can induce homogeneous crystallization inside the amorphous Al<sub>2</sub>O<sub>3</sub> film (9), which differs from the Al(OH)<sub>3</sub>/Al<sub>2</sub>O<sub>3</sub> bilayer configuration formed from the H<sub>2</sub>O exposure shown here at the electron flux of  $\sim 8300 \ e \ \text{Å}^{-2} \ \text{s}^{-1}$ . We also perform both the "low-dose" and "blank-beam" experiments to ensure that an intrinsic behavior is studied. With the use of the electron counting mode of a direct detection camera at the electron flux of  $<2300 e \text{ Å}^{-2} \text{ s}^{-1}$  to minimize the electron irradiation effects while maintaining the lattice resolution, the in situ TEM imaging clearly shows the Al (OH)<sub>3</sub>/Al<sub>2</sub>O<sub>3</sub> bilayer film growth (Fig. 2 and fig. S4). In addition, blank-beam experiments are also performed and demonstrate the Al(OH)<sub>3</sub>/Al<sub>2</sub>O<sub>3</sub> bilayer film formation on Al surfaces from the H<sub>2</sub>O exposure in the dark (fig. S5). Ex situ TEM observations are also performed to confirm the formation of the Al(OH)<sub>3</sub>/Al<sub>2</sub>O<sub>3</sub> bilayer structure outside the ETEM conditions. This is illustrated by ex situ TEM observations of an Al foil that is directly immersed

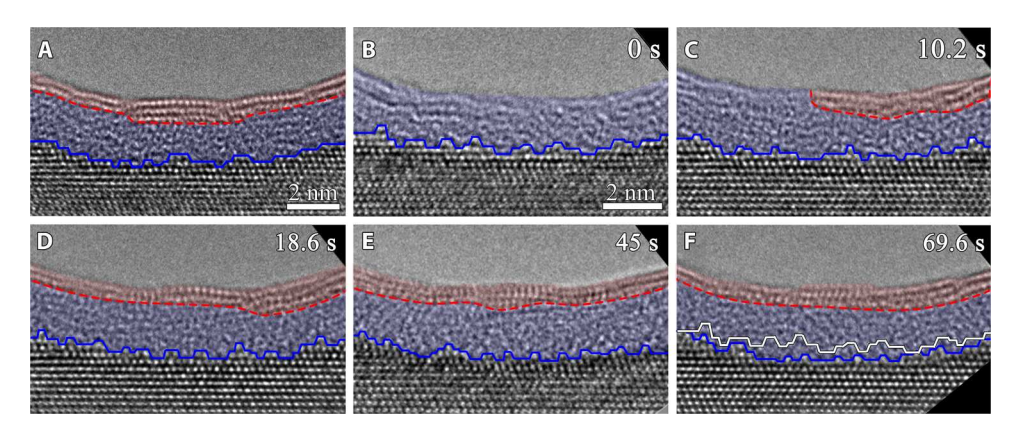
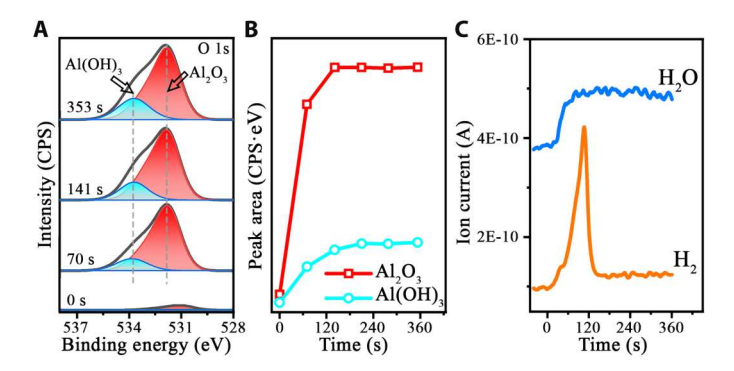


Fig. 4. Water vapor–induced Al(OH)<sub>3</sub> formation on an amorphous Al<sub>2</sub>O<sub>3</sub> overlayer. (A) HRTEM image of a Al(OH)<sub>3</sub>/Al<sub>2</sub>O<sub>3</sub> bilayer film on Al(111). (B) The Al(OH)<sub>3</sub> outer layer is largely sputtered off using the condensed electron beam. (C to F) Time-sequence HRTEM images showing the recovery of the Al(OH)<sub>3</sub>/Al<sub>2</sub>O<sub>3</sub> bilayer film configuration upon the hydroxylation of the amorphous Al<sub>2</sub>O<sub>3</sub> at 298 K in pH<sub>2</sub>O  $\approx 3.5 \times 10^{-4}$  torr. The dashed red and solid blue lines mark the Al(OH)<sub>3</sub>/Al<sub>2</sub>O<sub>3</sub> and Al<sub>2</sub>O<sub>3</sub>/Al(111) interfaces, respectively. The solid white line in (F) is the superimposed trace of the position and profile of the Al<sub>2</sub>O<sub>3</sub>/Al interface at t = 0 s in (B).

into DI liquid water, showing the formation of a bilayer structure consisting of a crystalline-like top layer and an inner amorphous layer (fig. S6), consistent with the Al(OH)<sub>3</sub>/Al<sub>2</sub>O<sub>3</sub> bilayer structure observed from the ETEM experiments. In addition, the effect of possible background gas molecules (such as H2, O2, water vapor, and carbonyl) in the TEM column is found to be negligible. This is confirmed by in situ TEM imaging, showing that the Al surfaces under vacuum (base pressure of  $8 \times 10^{-8}$  torr) maintain oxide-free for a relatively long period of time inside the TEM before flowing H<sub>2</sub>O vapor into the sample region (fig. S7). The effect of any residual O<sub>2</sub> in the TEM column is also confirmed to be insignificant, as shown by comparative in situ HRTEM imaging of the Al surfaces in  $3.5 \times 10^{-5}$  torr of H<sub>2</sub>O and O<sub>2</sub>, respectively, where the former leads to the Al(OH)<sub>3</sub>/Al<sub>2</sub>O<sub>3</sub> bilayer oxide film (Figs. 1 to 4), whereas the latter only forms an amorphous Al<sub>2</sub>O<sub>3</sub> layer (fig. S8). All the in situ and ex situ TEM observations confirm that the Al(OH)<sub>3</sub>/Al<sub>2</sub>O<sub>3</sub> bilayer film formation is an intrinsic feature for the H<sub>2</sub>O-induced surface passivation, irrespective of the electron beam irradiation, crystallographic orientations, and surface defects.



**Fig. 5. AP-XPS** and **RGA** measurements of the passive oxide film formation on **Al(111).** (**A**) Time-resolved photoemission spectra and intensity counts per second (CPS) of the O 1s core-level region obtained during the exposure of pristine Al(111) at 298 K to  $1 \times 10^{-5}$  torr of water vapor, where the faint peak intensity at 0 s can be attributed to the residual oxygen that cannot be completely removed by sputtering and annealing. (**B**) Time evolution of the integrated intensity of the Al<sub>2</sub>O<sub>3</sub> and Al(OH)<sub>3</sub> components. (**C**) Coordinated RGA measurements of the evolution of the feeding H<sub>2</sub>O (blue) and H<sub>2</sub> production (orange).

It can be also noted from the above in situ TEM imaging that the crystalline-like Al(OH)<sub>3</sub> can readily form on the amorphous Al<sub>2</sub>O<sub>3</sub> layer, irrespective of the surface morphology and orientation of the Al substrate. This easy formation of the crystalline Al(OH)<sub>3</sub> phase can be attributed to the underlying amorphous Al<sub>2</sub>O<sub>3</sub> layer, for which there is the absence of the epitaxial strain in the Al(OH)<sub>3</sub> overlayer. As a result, the crystalline phase of Al(OH)<sub>3</sub> is thermodynamically more favored than its amorphous counterpart. This is in contrast to the Al<sub>2</sub>O<sub>3</sub>/Al interface, where the crystalline Al substrate makes the formation of the crystalline Al<sub>2</sub>O<sub>3</sub> unfavorable due to their large lattice misfit. Instead, the amorphous Al<sub>2</sub>O<sub>3</sub> becomes more favorable to minimize the Al<sub>2</sub>O<sub>3</sub>/Al interface strain. Such an interface effect is in good accordance with the thermodynamics calculations, showing that the formation of the ultrathin amorphous Al<sub>2</sub>O<sub>3</sub> film is more favored than its crystalline counterpart from the oxidation of Al surfaces (30, 31).

## AP-XPS and RGA measurements of the AI surface passivation in H<sub>2</sub>O vapor

To cross-validate the in situ TEM observations, complementary ambient-pressure XPS (AP-XPS) is used to chemically confirm the formation of the Al(OH)<sub>3</sub>/Al<sub>2</sub>O<sub>3</sub> bilayer film from the H<sub>2</sub>O vapor exposure. Figure 5A illustrates time-resolved O 1s XPS spectra while exposing a clean Al(111) surface at 298 K to 1 ×  $10^{-5}$  torr of H<sub>2</sub>O vapor, showing the appreciable O 1s peak intensity after the H<sub>2</sub>O exposure. The O 1s exhibits the asymmetry to the high binding energy side and can be deconvoluted into two peaks with the binding energies of 532.1 and 533.8 eV. The peak at 532.1 eV is attributed to the O in Al-O bonds of Al<sub>2</sub>O<sub>3</sub>, whereas the other peak at 533.8 eV is consistent with the O in Al-OH bonds of Al(OH)<sub>3</sub> (29, 32–34). This corroborates well with the Al 2p spectra (fig. S9) that can be deconvoluted into metallic (Al<sup>0</sup>) at 72.8 eV and oxidized Al<sup>3+</sup> at 75.5 eV, respectively. It is worth mentioning that the binding energies for Al in Al<sub>2</sub>O<sub>3</sub> and Al(OH)<sub>3</sub> are 75.6 and 75.2 eV, respectively, which are too close to differentiate from the XPS measurements (29, 34, 35). Figure 5B corresponds to the integrated intensity evolution of O 1s spectra as a function of time, showing the dominant peak intensity by the Al<sub>2</sub>O<sub>3</sub> component and the rapid peak intensity growth to the saturated level for both the  $Al_2O_3$  and  $Al(OH)_3$  components. This is consistent with the in situ TEM imaging of the self-limiting Al oxide film growth that is dominated by the  $Al_2O_3$  growth at the  $Al_2O_3/Al$  interface, while the upper  $Al(OH)_3$  layer maintains a constant thickness. As revealed from the in situ TEM imaging (Figs. 1 to 3), the  $Al(OH)_3$  formation takes place within the first ~20 s of the  $H_2O$  exposure before the  $Al_2O_3$  growth. This sequential formation of  $Al(OH)_3$  and  $Al_2O_3$  cannot be detected readily by AP-XPS because of its long data acquisition time (~1 min) that results in the temporal summation of the overall signals from the probed surface area (~300  $\mu$ m).

Figure 5C illustrates the coordinated residual gas analyzer (RGA) measurements of the gas composition evolution during flowing the H<sub>2</sub>O vapor in the AP-XPS chamber. The measurement shows a spike of the H<sub>2</sub> production, while the feeding H<sub>2</sub>O vapor maintains at the constant pressure. The RGA results show that the H<sub>2</sub> product amount gradually increases to the maximum and then drops to zero after ~120 s of the H<sub>2</sub>O exposure, which is correlated well with the time period of reaching the limiting thickness of the oxide film measured by the O 1s spectra (Fig. 5A). Because the maximum H<sub>2</sub> production takes place after ~100 s of the H<sub>2</sub>O dosing (Fig. 5C), this suggests that the Al(OH)<sub>3</sub> surface termination is more reactive toward the H<sub>2</sub> formation than the pristine metallic Al surface. The termination of the H<sub>2</sub> production is attributed to the reached limiting thickness of the oxide film, for which the Al(OH)<sub>3</sub> surface restores its stoichiometry and thus loses its reactivity toward dissociative H<sub>2</sub>O adsorption, as described in our density functional theory (DFT) modeling below. It is also worth mentioning that the penetration of atomic H produced from the dissociative H<sub>2</sub>O adsorption into the deeper region below the Al(OH)3 layer can be negligible. This can be evidenced by the AP-XPS measurements (Fig. 5, A and B), which chemically confirm the dominant presence of the O peak compared to the OH peak. In addition, the coordinated RGA measurements show the production of gaseous H<sub>2</sub> before reaching the limiting thickness of the passivating film (Fig. 5C), indicating that the H from the dissociative H<sub>2</sub>O adsorption combines into molecular H<sub>2</sub> that desorbs from the surface rather than penetrates to the Al<sub>2</sub>O<sub>3</sub> region for hydrolysis to occur.

### Atomistic modeling of the passive oxide film formation

The in situ TEM observations and XPS results above are mutually consistent in providing strong evidence of the H2O-induced Al (OH)<sub>3</sub>/Al<sub>2</sub>O<sub>3</sub> bilayer film growth. The observed inward Al<sub>2</sub>O<sub>3</sub> growth at the Al<sub>2</sub>O<sub>3</sub>/Al interface along with the constant thickness of the top  $Al(OH)_3$  layer suggests that the oxidation is dominated by the inward migration of O from the top Al(OH)<sub>3</sub> layer to the Al<sub>2</sub>O<sub>3</sub>/ Al interface and the outward Al diffusion is negligible. To shed light on the microscopic mechanism of the bilayer film growth, reactive force-field (ReaxFF) molecular dynamics (MD) simulations are performed to examine the surface reaction between Al surfaces and H<sub>2</sub>O vapor. Figure 6 (A to G) shows the simulation snapshots captured at different H<sub>2</sub>O exposure times of the Al(100) surface. As shown in the snapshot of 300 ps of H<sub>2</sub>O exposure (Fig. 6A), Al—OH bonds are formed in the oxide layer, which indicates the dissociation of H<sub>2</sub>O into OH<sup>-</sup> and H<sup>+</sup> to result in the surface hydroxylation, consistent with the in situ TEM observations of the direct Al(OH)<sub>3</sub> formation on pristine Al surfaces (Figs. 1 and 2). Figure 6A also shows the penetration of atomic H into the Al lattice, which is caused by the use of the Berendsen thermostat (36) to accelerate the notably slow dissociation of H<sub>2</sub>O molecules at room temperature in the MD simulations (37–39). This approach

was used in previous studies to investigate the interactions between H<sub>2</sub>O molecules and the Al surface (36, 40). Figure 6B illustrates a presentative Al—(OH) bond configuration resulting from the H<sub>2</sub>O exposure, showing that the Al—OH bond lengths range from 1.90 to 1.98 Å, and the Al—O—H bond angles fall into the range of 128.4° to 176.9°, which are close to the corresponding bond length (1.88 to 1.97 Å) and bond angle (105.1° to 121.7°) in bulk Al(OH)<sub>3</sub> (Fig. 6C). However, it also needs to be mentioned that the produced Al—OH bond angles fall into a larger range than that of bulk Al (OH)<sub>3</sub> because the Al—OH bonds in the surface oxide layer are more defective than the ordered arrangement of bulk Al(OH)<sub>3</sub>.

Figure 6 (D and E) shows the displacement vectors of O and Al atoms between 1 and 70 ps, which correspond to the initial-stage surface hydroxylation by H<sub>2</sub>O molecules. As can be seen in Fig. 6D, nearly all the displacement vectors of O atoms point inward, which indicates inward migration of O atoms toward the Al substrate. In contrast, the displacement vectors of Al atoms in the oxygenated region largely point outward (Fig. 6E), indicating the outward relaxation of Al atoms due to the embedment of O atoms into the Al lattice at the Al<sub>2</sub>O<sub>3</sub>/Al interface. Figure 6 (F and G) shows the displacement vectors of O and Al atoms between 201 and 300 ps, corresponding to a relatively later stage of the H<sub>2</sub>O exposure. As shown in Fig. 6F, the O atoms still display the inward displacements, which indicates the embedment of more O atoms into the Al lattice and corresponds to the tendency of forming an inner Al<sub>2</sub>O<sub>3</sub> layer. The number of Al-OH bonds remains nearly constant after 220 ps of H<sub>2</sub>O exposure. This indicates the trend of approaching a constant thickness of the Al hydroxide outer layer, agreeing well with the in situ TEM observations of the constant thickness of the Al(OH)<sub>3</sub> layer (Figs. 1 to 3 and fig. S2 and S4). The displacement vectors of Al atoms (Fig. 6G) show slight outward relaxations induced by the continued O embedment into the Al substrate.

To further elucidate the surface nature of the Al hydroxide formation in H<sub>2</sub>O, ReaxFF MD simulations of the surface oxidation of Al(100) are performed sequentially, first in  $O_2$  and then switching to  $H_2O$ . That is, pristine Al(100) is first exposed to  $O_2$  to result in the formation of an amorphous Al oxide layer after 100 ps of the canonical relaxation under the conditions of a constant particle number (N), constant volume (V), and constant temperature (T) (NVT). The  $O_2$ -generated Al(100) slab is then used to simulate the dissociative adsorption of H<sub>2</sub>O molecules via the same procedure as that in the H<sub>2</sub>O exposure simulation mentioned above. Figure 6H displays a simulation snapshot after 100 ps of the H<sub>2</sub>O exposure, showing the formation of Al-OH bonds dominated in the outermost surface region. This is consistent with the in situ TEM observation (Fig. 4), showing the formation of a Al(OH)<sub>3</sub> layer on the amorphous Al<sub>2</sub>O<sub>3</sub> layer from the subsequent H<sub>2</sub>O exposure. Figure 6 (I and J) illustrates the displacement vectors of O and Al atoms between 0 and 100 ps, corresponding to the H<sub>2</sub>O exposure to the O<sub>2</sub>-generated Al(100) slab. As shown in Fig. 6I, the O atoms still show the inward displacements, which indicates the continued incorporation of dissociated O atoms into the Al lattice from the surface adsorbed H<sub>2</sub>O, thereby resulting in the inward migration of the Al<sub>2</sub>O<sub>3</sub>/Al interface. Figure 6J displays the displacement vectors of Al atoms showing the slight outward relaxations due to the continued O embedment into the Al substrate.

Last, we illustrate the atomic origin leading to the  $Al(OH)_3/Al_2O_3$  bilayer film growth in  $H_2O$ . Our in situ TEM observations

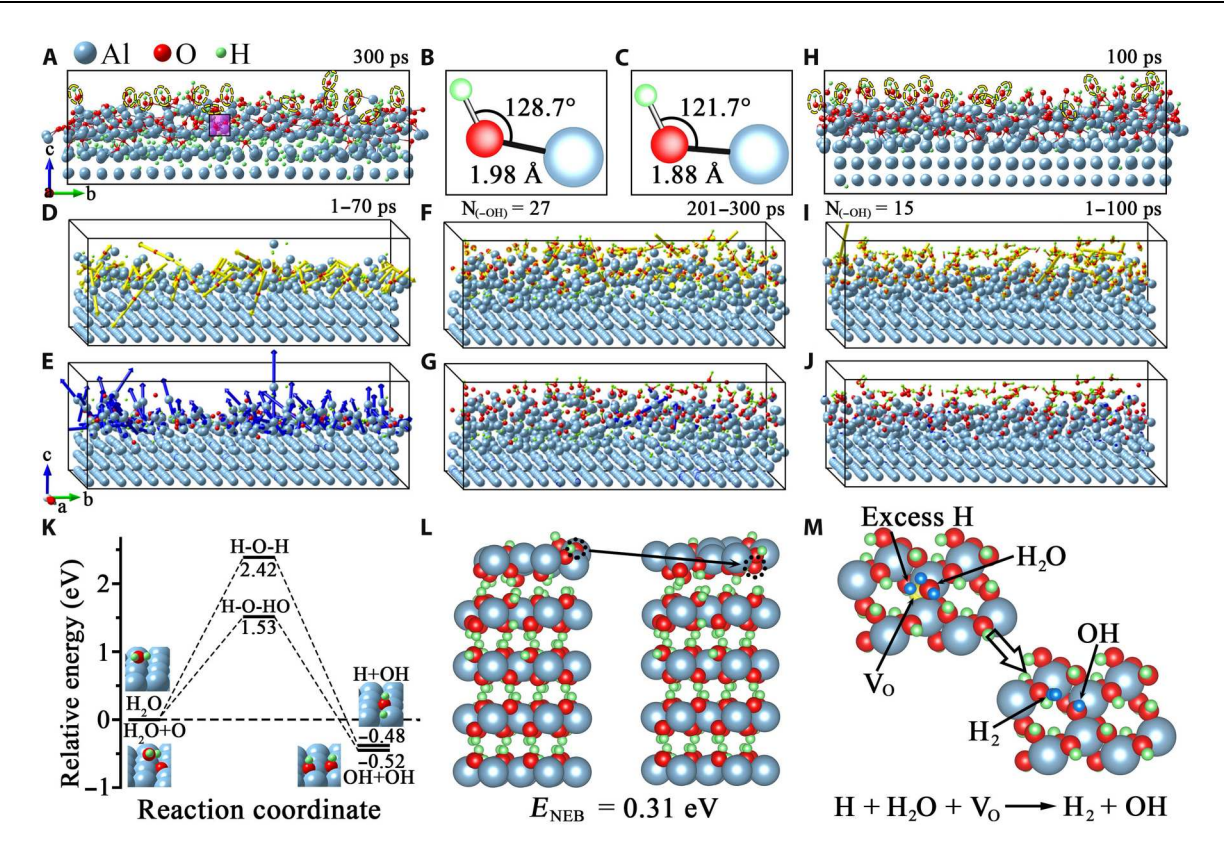


**Fig. 6. ReaxFF MD and DFT simulations of water vapor–induced surface passivation.** (**A**) Snapshot of MD simulations of a Al(100) surface after 300 ps of  $H_2O$  exposure at 298 K (movies S5 to S7). (**B**) Al—O—H bonding configuration of the purple-shaded region in (A) and its comparison to that of bulk Al(OH)<sub>3</sub> in (**C**). (**D** and **E**) Displacement vectors of O and Al atoms between 1 and 70 ps of  $H_2O$  exposure. (**F** and **G**) Displacement vectors of O and Al atoms between 201 and 300 ps of  $H_2O$  exposure. (**H**) Snapshot of MD simulation of a preoxidized Al(100) surface after 100 ps of  $H_2O$  exposure at 298 K (movie S8). (**I** and **J**) MD simulations of  $H_2O$ -induced hydroxylation and displacement vectors of O and Al atoms between 1 and 100 ps of  $H_2O$  exposure of an  $H_2O$  overlayer formed by the exposure of Al(100) at 298 K to  $H_2O$ . The dashed yellow circles in (A) and (H) mark the formed hydroxyl on the surface. (**K** and **L**) Nudged elastic band (NEB) modeling of the dissociation pathways and energy barriers for  $H_2O$  dissociation on Al(111) and the migration of surface O to an O vacancy site in the subsurface of the bulk-truncated Al(OH)<sub>3</sub>(001), respectively. (**M**) DFT modeling of the dissociation pathway for the adsorbed  $H_2O$  on the defective Al(OH)<sub>3</sub>(001) surface with the presence of an O vacancy and excess H at the surface.

and MD simulation above have shown that the  $H_2O$ -induced surface passivation occurs via a two-stage process: first the Al  $(OH)_3$  formation via  $H_2O$  dissociation into OH groups for the Al  $(OH)_3$  formation followed by  $Al_2O_3$  growth through inward O diffusion. This implies a difference in the reaction pathway for the pristine Al surface and the  $Al(OH)_3$  terminated surface. DFT calculations are performed to evaluate this difference in the dissociation pathways of  $H_2O$  molecules. As shown in Fig. 6K, our DFT calculations show that it is energetically favorable for the dissociation of a  $H_2O$  molecule on Al(111) into  $OH^-$  and  $H^+$  by overcoming an energy barrier of  $\sim 2.42$  eV, and the presence of preadsorbed O on the surface (formed due to the presence of any residual  $O_2$  in the surrounding) can reduce the energy barrier to  $\sim 1.53$  eV. This is in good accordance with other DFT studies showing the preferential OH formation of  $H_2O$  molecules on pristine Al surfaces (41-43).

For the  $Al(OH)_3$  surface, our DFT calculations show that the perfect, stoichiometric surface does not show any activity toward dissociative  $H_2O$  adsorption. As informed from our in situ TEM observations, the  $Al_2O_3$  growth occurs at the  $Al_2O_3/Al$  interface, which requires the supply of O ions from the top  $Al(OH)_3$  layer to the inner interface. The diffusion energy barrier for such inward migration of O ions from the  $Al(OH)_3$  surface to an O

vacancy site in the subsurface is calculated to be 0.31 eV (Fig. 6L). This small diffusion energy barrier suggests that the inward diffusion of O ions across the Al(OH)<sub>3</sub> layer is kinetically achievable. Therefore, this inward Al<sub>2</sub>O<sub>3</sub> growth results in O vacancies (V<sub>O</sub>) and excess H at the Al(OH)3 surface, which may facilitate the dissociative adsorption of H<sub>2</sub>O. Our DFT calculations show that the molecular H<sub>2</sub>O placed slightly above the O vacancy site results in its spontaneous dissociation into H<sup>+</sup> and OH<sup>-</sup>, where the former bonds with adjacent excess H to form a H<sub>2</sub> molecule that desorbs from the surface, whereas the latter occupies the original VO site (Fig. 6M). The DFT modeling also explains why the Al(OH)<sub>3</sub> layer stays as the top layer because it is in direct contact with the H<sub>2</sub>O vapor, where the dissociative H<sub>2</sub>O adsorption provides OH species to maintain the Al(OH)<sub>3</sub> structure in addition to the H<sub>2</sub> production. The process of the inward O migration and H<sub>2</sub>O dissociative adsorption at the Vo sites repeats itself until the oxide film reaches its limiting thickness, at which the termination of the Al<sub>2</sub>O<sub>3</sub> growth leads to the restoration of the surface stoichiometry of the Al(OH)<sub>3</sub> layer. As a result, the Al(OH)<sub>3</sub> surface loses its reactivity toward further dissociative H<sub>2</sub>O adsorption.

### **DISCUSSION**

The wide use of Al is attributed to its ability to form a passivation layer that is typically assumed to have an amorphous structure in nature (44-47). As shown above, our in situ TEM imaging clearly demonstrates that the passivating layer on Al surfaces in water consists of a crystalline Al(OH)<sub>3</sub> outer layer and an amorphous Al<sub>2</sub>O<sub>3</sub> inner layer. This Al(OH)<sub>3</sub>/Al<sub>2</sub>O<sub>3</sub> bilayer configuration not only differs microstructurally from the surface passivation in dry O<sub>2</sub> that results in a single layer of amorphous Al<sub>2</sub>O<sub>3</sub> (see the example in fig. S8) but also alters the passivating film growth mechanism from both inward O diffusion and outward Al diffusion in O2 (10) to the inward O diffusion in H<sub>2</sub>O. The inward O diffusion for Al<sub>2</sub>O<sub>3</sub> growth at the Al<sub>2</sub>O<sub>3</sub>/Al interface results in V<sub>O</sub> and excess H at the crystalline Al(OH)3 overlayer, which promotes the H<sub>2</sub> production from the dissociative H<sub>2</sub>O adsorption. This insight may have important implications for the design of materials in clean-energy and environmental applications. For instance, Al has been proposed for onboard vehicular H2 storage for making clean  $H_2$  from the reaction between Al and  $H_2O$  (48–50). Our results shown above provide the mechanistic insight into this reaction by identifying the important role of the Al(OH)<sub>3</sub> formation for the H<sub>2</sub> production from H<sub>2</sub>O. That is, the Al(OH)<sub>3</sub> overlayer serves as a catalyst to promote the reaction pathway of H +  $H_2O$  +  $V_O$   $\rightarrow$  $OH + H_2$  at ambient temperature. On the other hand, the corrosion of metallic materials in humid environments is encountered in daily life due to the ubiquity of water. The atomistic mechanisms identified from the passivating film formation on Al surfaces in H<sub>2</sub>O may find applicability to understand the microscopic mechanisms controlling the surface passivating dynamics of other metals under humid conditions.

Using a combination of in situ TEM and atomistic modeling, we provide direct evidence that the surface passivation of Al surfaces in water vapor results in the formation of an Al(OH)<sub>3</sub>/Al<sub>2</sub>O<sub>3</sub> bilayer film. The Al(OH)<sub>3</sub> outer layer has a crystalline structure and maintains a constant thickness, while the inner amorphous Al<sub>2</sub>O<sub>3</sub> layer grows at the Al<sub>2</sub>O<sub>3</sub>/Al interface to a limiting thickness. Such bilayer passivating film growth is related to the two-stage passivation reaction: first, the H<sub>2</sub>O dissociation into OH + H on the pristine Al surface to form the Al(OH)3 overlayer and, then, into OH + H2 on the O-deficient Al(OH)3 overlayer due to inward O diffusion to the Al<sub>2</sub>O<sub>3</sub>/Al interface. These fundamental insights demonstrate the tunability of the dissociation pathways of H2O molecules and have practical implications not only in controlling the microscopic processes of the passivating film growth but also in clean H2 production from H<sub>2</sub>O catalyzed by the spontaneously formed Al hydroxide overlayer on Al.

### **MATERIALS AND METHODS**

### Sample preparation

Thin Al foils with a nominal thickness of ~50 nm are prepared using the focused ion beam (FIB) lift-out technique (FEI Helios Nanolab 600) and the NanoMill system. To minimize potential surface damage and Ga contamination, the ion beam with a low voltage (5 kV) and current (9 pA) is used to do the final trimming of the surface of the sliced sample during the FIB process. Thereafter, the Al slice is loaded on a Mo Omniprobe Lift-out grid and further polished by the NanoMill TEM specimen preparation system with a

lower voltage (900 V) and current (80 pA) of Ar<sup>+</sup> ions to remove the possible surface damage and contamination. The as-prepared Al thin foils are then examined by HRTEM imaging and chemical analyses, confirming that the structure damage and contamination from the FIB process are negligible (figs. S10 and S11).

### In situ HRTEM experiments

In situ TEM experiments are performed using an image-corrected environmental TEM (FEI Titan 80-300) operated at 300 kV, which is equipped with a differential pumping system. The microscope has a spatial resolution of 0.8 Å in the HRTEM mode. Atomically clean Al surfaces are obtained using a condensed electron beam inside the TEM column to sputter off native oxide and generate well-defined facets with a thickness (~50 nm) (9). These freshly generated facets are oxide-free and ideal for in situ TEM observations of water vapor-induced surface passivation from the beginning (see more details in fig. S1). The in situ HRTEM images are captured with a positive Cs value (1 to 3 µm). Complete removal of the native oxide and surface cleanliness are confirmed by HRTEM imaging, electron diffraction, and electron energy loss spectroscopy. Water vapor is then introduced into the sample area through a leak valve to oxidize the Al foils at a given temperature and gas pressure. In situ TEM observations of the passivation process are made in the cross-sectional views by imaging along surface facets. The in situ TEM movies are drift-corrected to ensure the same sample area in the field of view.

### **HRTEM** image simulations

The DFT-relaxed atomic structure models of Al and Al(OH)<sub>3</sub> are used as input files for HRTEM image simulations. HRTEM image simulations are performed using the multislice method with the parameters carefully matched to the experimental conditions (accelerating voltage, 300 keV; the spherical aberration, 0.001 mm; defocus, –8 nm; and thickness, 28 nm). The frozen phonon model is applied to reduce the elastic scattering and increase the background intensity.

### In situ AP-XPS experiments

XPS measurements are performed within an ultrahigh vacuum system. The system is equipped with an XPS spectrometer (SPECS Phoibos 150 MCD analyzer) with a delay-line detector, and an Ar-ion sputtering gun. The chamber has a base pressure of  $1.5\times10^{-10}$  torr. Al-K $\alpha$  x-ray radiation is used for the XPS measurements. The Al(111) single crystal is a "top-hat" disk (1-mm thick and 8 mm in diameter), purchased from Princeton Scientific Corp., cut to within 0.1° to the (111) crystallographic orientation, and polished to a mirror finish. The crystal is cleaned by cycles of Ar $^+$  bombardment at 298 K and annealing to 700 K. Water vapor (purity, 99.9999%) is introduced to the system through a leak valve, and the sample is oxidized at 298 K with a water vapor pressure of 1  $\times$   $10^{-5}$  torr.

### **ReaxFF MD simulations**

MD simulations are performed using the LAMMPS code (45). The bonding, angle, and torsion between the Al, H, and O atoms are described using the ReaxFF interatomic potential, which was developed by Van Duin and colleagues (51–53). A periodic supercell with the Al(001) surface and H<sub>2</sub>O molecules is used to simulate the surface passivation of Al under water vapor. The Al(001)

surface is modeled as a 4.04 nm-by-4.04 nm-by-2.83 nm slab, with a vacuum space of 10 nm added above the slab surface to separate each periodic image. First, the Al slab is relaxed with an NPT [a fixed number of particles (N), and constant pressure (P), and temperature (T)] ensemble at 298 K and 1 atm until it reaches a stable structure. Then, 72 H<sub>2</sub>O molecules (16.5 mg/cm<sup>3</sup>) are randomly distributed near the surface, avoiding overlap. Afterward, an NVT ensemble simulation is performed at room temperature on the Al slab and H<sub>2</sub>O molecules for 70 ps with a time step of 0.1 fs, resulting in a stable structure with H<sub>2</sub>O molecules situated on the Al(001) surface. Subsequently, microcanonical ensemble simulations are performed for 100 ps to simulate the water dissociation and surface passivation reactions. Given that the dissociation of H<sub>2</sub>O molecules on the Al slab surface is notably slow, we use the Berendsen velocity scaling thermostat with a damping constant of 100 fs to enhance the reaction rate in the microcanonical ensemble simulation (39). We separate the system into two temperature zones: the Al slab, which is treated as a heat sink with a target temperature of 0 K, and the remaining particles, which are accelerated to a target temperature of 1650 K (36). We repeat the process of adding H<sub>2</sub>O molecules and conducting subsequent canonical ensemble and microcanonical ensemble simulations three times, a process that we refer to as a three-stage procedure. We use the last trajectory from each stage as the initial structure for the subsequent stage. This approach of accelerating the H<sub>2</sub>O dissociation process was used in the previous study in investigating the interactions between H<sub>2</sub>O molecules and Al nanoparticles (36, 39).

### **DFT** calculations

DFT calculations are performed using the Vienna Ab initio Simulation Package (54, 55) with the Perdew-Burke-Ernzerhof generalized gradient approximation and projector augmented wave potentials (56, 57). The cutoff energies of 400 and 600 eV are used to calculate the adsorption energies. Their resulting differences are less than 0.1 eV, confirming that the cutoff energy of 400 eV is sufficient for the electronic energy convergence. The  $(4 \times 4 \times 1)$  Kpoint meshes based on Monkhorst-Pack grids are applied for the Brillouin zone integration. The convergence test for the *K*-points mesh is performed by comparing the adsorption energy difference between the  $(4 \times 4 \times 1)$  and  $(8 \times 8 \times 1)$  meshes, which suggests that the  $(8 \times 8 \times 1)$  mesh gives an adsorption energy difference of less than 0.1 eV, indicating that convergence criterion is reached using the  $(4 \times 4 \times 1)$  mesh. Al(111) and Al(OH)<sub>3</sub> surfaces are constructed by cleaving supercells made from bulk structure. Successive slabs with five atomic layers are separated by a vacuum region of 12 Å. The positions of the atoms in the two bottom layers are fixed, while the positions of the atoms in the top three layers are allowed to relax with the energy convergence less than  $\sim 10^{-5}$  eV and all force components on each of them are less than 0.015 eV/ Å. We investigate the adsorption energies of H<sub>2</sub>O, OH, and H species on surfaces and structure evolution for each calculation. Furthermore, the diffusion energy barrier for the incorporation of O on Al(OH)<sub>3</sub> surface into the subsurface region is calculated using the nudged elastic band method. The atomic structures are visualized using the Visualization for Electronic and Structure Analysis.

### **Supplementary Materials**

This PDF file includes:

Supplementary Text Figs. S1 to S11 Legends for movies S1 to S8

Other Supplementary Material for this manuscript includes the following:
Movies S1 to S8

### REFERENCES AND NOTES

- B. N. Zope, D. D. Hibbitts, M. Neurock, R. J. Davis, Reactivity of the gold/water interface during selective oxidation catalysis. Science 330, 74–78 (2010).
- 2. B. C. H. Steele, A. Heinzel, Materials for fuel-cell technologies. Nature 414, 345–352 (2001).
- R. S. Dutta, Corrosion aspects of Ni-Cr-Fe based and Ni-Cu based steam generator tube materials. J. Nucl. Mater. 393, 343–349 (2009).
- C. Costentin, D. G. Nocera, Self-healing catalysis in water. Proc. Natl. Acad. Sci. U.S.A. 114, 13380–13384 (2017).
- L. Ma, E. M. Pascalidou, F. Wiame, S. Zanna, V. Maurice, P. Marcus, Passivation mechanisms and pre-oxidation effects on model surfaces of FeCrNi austenitic stainless steel. *Corros. Sci.* 167, 108483 (2020).
- S. Maier, M. Salmeron, How does water wet a surface? Acc. Chem. Res. 48, 2783–2790 (2015).
- J. Guo, X. Meng, J. Chen, J. Peng, J. Sheng, X. Z. Li, L. Xu, J. R. Shi, E. Wang, Y. Jiang, Real space imaging of interfacial water with submolecular resolution. *Nat. Mater.* 13, 184–189 (2014).
- 8. Y. Yang, A. Kushima, W. Han, H. Xin, J. Li, Liquid-like, self-healing aluminum oxide during deformation at room temperature. *Nano Lett.* **18**, 2492–2497 (2018).
- L. Nguyen, T. Hashimoto, D. N. Zakharov, E. A. Stach, A. P. Rooney, B. Berkels, G. E. Thompson, S. J. Haigh, T. L. Burnett, Atomic-scale insights into the oxidation of aluminum. ACS Appl. Mater. Interfaces 10, 2230–2235 (2018).
- X. Chen, Z. Liu, D. Wu, N. Cai, X. Sun, D. N. Zakharov, S. Hwang, D. Su, G. Wang, G. Zhou, Passive oxide film growth observed on the atomic scale. *Adv. Mater. Interfaces* 9, 2102487 (2022).
- J. D. Holladay, Y. Wang, E. Jones, Review of developments in portable hydrogen production using microreactor technology. Chem. Rev. 104, 4767–4790 (2004).
- H. Z. Wang, D. Y. C. Leung, M. K. H. Leung, M. Ni, A review on hydrogen production using aluminum and aluminum alloys. *Renew. Sustain. Energy Rev.* 13, 845–853 (2009).
- T. Zhang, W. Yang, S. Zhang, J. Zhou, J. Liu, Hydrogen production by the reaction of Albased metals with water vapor. *Energy Sources Part A Recovery Util. Environ. Eff.* 40, 9–14 (2018)
- A. M. Thron, J. Gao, B. Ercan, M. A. Laurent, S. Chowdhury, K. van Benthem, Oxidation behavior of InAIN during rapid thermal annealing. *Phys. Status Solidi.* 218, 2100304 (2021).
- T. L. Barth, E. A. Marquis, Effects of minor alloying elements on alumina transformation during the transient oxidation of β-NiAl. Oxid. Met. 95, 293–309 (2021).
- Q. Liu, L. Li, N. Cai, W. A. Saidi, G. Zhou, Oxygen chemisorption-induced surface phase transitions on Cu(110). Surf. Sci. 627, 75–84 (2014).
- J. S. Lee, T. Kaufman-Osborn, W. Melitz, S. Lee, A. Kummel, Effect of H<sub>2</sub>O chemisorption on passivation of Ge(100) surface studied by scanning tunneling microscopy. Surf. Sci. 605, 1583–1588 (2011).
- Y. J. Kim, D. Kim, Y. Kim, Y. Jeong, B. Jeong, J. Y. Park, Effect of water vapor on oxidation processes of the Cu(111) surface and sublayer. *Int. J. Mol. Sci.* 24, 810 (2023).
- Y. Zhu, D. Wu, C. Li, X. Tong, J. A. Boscoboinik, J. T. Sadowski, G. Zhou, Atomistic mechanisms of the initial oxidation of stepped Cu<sub>3</sub>Au(100). *Phys. Rev. B.* 105, 075422 (2022).
- Q. Zhu, Z. Pan, Z. Zhao, G. Cao, L. Luo, C. Ni, H. Wei, Z. Zhang, F. Sansoz, J. Wang, Defect-driven selective metal oxidation at atomic scale. *Nat. Commun.* 12, 558 (2021).
- 21. C. L. Huang, W. L. Weng, C. N. Liao, K. N. Tu, Suppression of interdiffusion-induced voiding in oxidation of copper nanowires with twin-modified surface. *Nat. Commun.* **9**, 340 (2018).
- A. Vyalikh, K. Zesewitz, U. Scheler, Hydrogen bonds and local symmetry in the crystal structure of gibbsite. Magn. Reson. Chem. 48, 877–881 (2010).
- J. Frenzel, A. F. Oliveira, H. A. Duarte, T. Heine, G. Seifert, Structural and electronic properties of bulk gibbsite and gibbsite surfaces. *Zeitschrift fur Anorg. und Allg. Chemie.* 631, 1267–1271 (2005).
- S. Fleming, A. Rohl, M. Y. Lee, J. Gale, G. Parkinson, Atomistic modelling of gibbsite: Surface structure and morphology. J. Cryst. Growth 209, 159–166 (2000).

### SCIENCE ADVANCES | RESEARCH ARTICLE

- L. P. H. Jeurgens, W. G. Sloof, F. D. Tichelaar, E. J. Mittemeijer, Structure and morphology of aluminium-oxide films formed by thermal oxidation of aluminium. *Thin Solid Films* 418, 89–101 (2002).
- N. Cabrera, N. F. Mott, Theory of the oxidation of metals. Rep. Prog. Phys. 12, 163–184 (1949).
- N. Cai, G. Zhou, K. Müller, D. E. Starr, Tuning the limiting thickness of a thin oxide layer on Al (111) with oxygen gas pressure. *Phys. Rev. Lett.* 107, 035502 (2011).
- N. Cai, G. Zhou, K. Müller, D. E. Starr, Temperature and pressure dependent Mott potentials and their influence on self-limiting oxide film growth. Appl. Phys. Lett. 101, 171605 (2012).
- N. Cai, G. Zhou, K. Müller, D. E. Starr, Comparative study of the passivation of Al(111) by molecular oxygen and water vapor. J. Phys. Chem. C 117, 172–178 (2013).
- L. P. H. Jeurgens, W. G. Sloof, F. D. Tichelaar, E. J. Mittemeijer, Thermodynamic stability of amorphous oxide films on metals: Application to aluminum oxide films on aluminum substrates. *Phys. Rev. B.* 62, 4707 (2000).
- M. Aykol, K. A. Persson, Oxidation protection with amorphous surface oxides: Thermodynamic insights from Ab initio simulations on aluminum. ACS Appl. Mater. Interfaces 10, 3039–3045 (2018).
- Q. Liu, H. Qin, J. A. Boscoboinik, G. Zhou, Comparative study of the oxidation of NiAl(100) by molecular oxygen and water vapor using ambient-pressure x-ray photoelectron spectroscopy. *Langmuir* 32, 11414–11421 (2016).
- A. Shavorskiy, K. Müller, J. T. Newberg, D. E. Starr, H. Bluhm, Hydroxylation of ultrathin Al<sub>2</sub>O<sub>3</sub>/NiAl(110) films at environmental humidity. *J. Phys. Chem. C* 118, 29340–29349 (2014).
- N. Cai, Q. Liu, X. Tong, G. Zhou, X-ray photoelectron spectroscopy study of the passivation of NiAl(100) by water vapor. *Langmuir* 30, 774–783 (2014).
- J. Zähr, S. Oswald, M. Türpe, H. J. Ullrich, U. Füssel, Characterisation of oxide and hydroxide layers on technical aluminum materials using XPS. Vacuum 86, 1216–1219 (2012).
- M. F. Russo, R. Li, M. Mench, A. C. T. Van Duin, Molecular dynamic simulation of aluminumwater reactions using the ReaxFF reactive force field. *Int. J. Hydrog. Energy* 36, 5828–5835 (2011).
- 37. R. K. Dong, Z. Mei, F. Q. Zhao, S. Y. Xu, X. H. Ju, Molecular dynamics simulation on the reaction of nano-aluminum with water: Size and passivation effects. *RSC Adv.* **9**, 41918–41926 (2019)
- Y. Zhao, D. X. Ma, F. Q. Zhao, S. Y. Xu, X. H. Ju, Atomic insights into the combustion behavior of Al nano-droplets with H<sub>2</sub>O vapor at high temperature. *Appl. Surf. Sci.* 586, 152777 (2022).
- H. J. C. Berendsen, J. P. M. Postma, W. F. Van Gunsteren, A. Dinola, J. R. Haak, Molecular dynamics with coupling to an external bath. J. Chem. Phys. 81, 3684–3690 (1984).
- S. Kumar, R. K. Sahu, Aluminum nanotubes as an efficient catalyst for hydrogen production via thermochemical water splitting: A reactive molecular dynamics simulation. *Phys. Chem. Chem. Phys.* 25, 13487–13497 (2023).
- F. Y. Guo, C. G. Long, J. Zhang, Z. Zhang, C. H. Liu, K. Yu, Adsorption and dissociation of H<sub>2</sub>O on Al(1 1 1) surface by density functional theory calculation. *Appl. Surf. Sci.* 324, 584–589 (2015).
- X. Wei, C. Dong, Z. Chen, K. Xiao, X. Li, A DFT study of the adsorption of O<sub>2</sub> and H<sub>2</sub>O on Al (111) surfaces. RSC Adv. 6, 56303–56312 (2016).
- J. E. Crowell, J. G. Chen, D. M. Hercules, J. T. Yates Jr., The adsorption and thermal decomposition of water on clean and oxygen-predosed Al(111). J. Chem. Phys. 86, 5804–5815 (1987).
- 44. F. Reichel, L. P. H. Jeurgens, E. J. Mittemeijer, The thermodynamic stability of amorphous oxide overgrowths on metals. *Acta Mater.* **56**, 659–674 (2008).

- D. Flötotto, Z. M. Wang, L. P. H. Jeurgens, E. J. Mittemeijer, Intrinsic stress evolution during amorphous oxide film growth on Al surfaces. Appl. Phys. Lett. 104, 091901 (2014).
- G. Kresse, M. Schmid, E. Napetschnig, P. Varga, M. Shishkin, L. Ko, Structure of the ultrathin aluminum oxide film on NiAl(110). Science 308, 1440–1442 (2005).
- S. K. Lee, S. B. Lee, S. Y. Park, Y. S. Yi, C. W. Ahn, Structure of amorphous aluminum oxide. Phys. Rev. Lett. 103, 095501 (2009).
- 48. S. Elitzur, V. Rosenband, A. Gany, Study of hydrogen production and storage based on aluminum-water reaction. *Int. J. Hydrog. Energy* **39**, 6328–6334 (2014).
- F. Xiao, R. Yang, Z. Liu, Active aluminum composites and their hydrogen generation via hydrolysis reaction: A review. *Int. J. Hydrog. Energy* 47, 365–386 (2022).
- X. Chen, C. Wang, Y. Liu, Y. Shen, Q. Zheng, S. Yang, H. Lu, H. Zou, K. Lin, H. Liu, H. Qiu, J. Wu,
   Q. Zhang, X. Liu, Popcorn-like aluminum-based powders for instant low-temperature water vapor hydrogen generation. *Mater. Today Energy* 19, 100602 (2021).
- Q. Zhang, T. Çağln, A. Van Duin, W. A. Goddard, Y. Qi, L. G. HectorJr., Adhesion and nonwetting-wetting transition in the Al/α-Al<sub>2</sub>O<sub>3</sub> interface. *Phys. Rev. B.* 69, 045423 (2004).
- J. G. O. Ojwang, R. Van Santen, G. J. Kramer, A. C. T. Van Duin, W. A. Goddard, Predictions of melting, crystallization, and local atomic arrangements of aluminum clusters using a reactive force field. *J. Chem. Phys.* 129, 244506 (2008).
- J. G. O. Ojwang, R. A. Van Santen, G. J. Kramer, A. C. T. Van Duin, W. A. Goddard III, Parametrization of a reactive force field for aluminum hydride. *J. Chem. Phys.* 131, 044501 (2009).
- G. Kresse, J. Hafner, Ab initio molecular-dynamics simulation of the liquid-metal–amorphous-semiconductor transition in germanium. *Phys. Rev. B.* 49, 14251–14269 (1994).
- G. Kresse, J. Hafner, Ab initio molecular dynamics for liquid metals. Phys. Rev. B. 47, 558–561 (1993).
- G. Kresse, J. Furthmüller, J. Hafner, Ab initio force constant approach to phonon dispersion relations of diamond and graphite. Europhys. Lett. 32, 729–734 (1995).
- G. Kresse, J. Furthmüller, Efficiency of ab-initio total energy calculations for metals and semiconductors using a plane-wave basis set. Comput. Mater. Sci. 6, 15–50 (1996).

### Acknowledgments

Funding: This work was supported by the U.S. Department of Energy (DOE), Office of Basic Energy Sciences, Division of Materials Sciences and Engineering under award no. DE-SC0001135. This research used resources of the Center for Functional Nanomaterials and the Scientific Data and Computing Center, a component of the Computational Science Initiative, which is a U.S. DOE Office of Science Facility, at Brookhaven National Laboratory under contract no. DE-SC0012704, G.W. acknowledges the financial support from the National Science Foundation under DMR 1905572/1905422 for the computational work, This research also used the computational resources provided by the University of Pittsburgh Center for Research Computing and the Extreme Science and Engineering Discovery Environment (XSEDE) supported by National Science Foundation grant number OCI-1053575. Author contributions: G.Z. and X.C. conceived and designed the experiments, X.C., S.B.P., and N.C. performed the experiments. W.S. and G.W. performed MD simulations, and D.W. conducted DFT calculations. G.Z. and X.C. analyzed data and wrote the paper. All the authors commented on the manuscript. Competing interests: The authors declare that they have no competing interests. Data and materials availability: All data needed to evaluate the conclusions in the paper are present in the paper and/or the Supplementary Materials.

Submitted 12 March 2023 Accepted 29 September 2023 Published 1 November 2023 10.1126/sciadv.adh5565

# Downloaded from https://www.science.org at University of Pittsburgh on December 15, 2023



### Atomistic mechanisms of water vapor-induced surface passivation

Xiaobo Chen, Weitao Shan, Dongxiang Wu, Shyam Bharatkumar Patel, Na Cai, Chaoran Li, Shuonan Ye, Zhao Liu, Sooyeon Hwang, Dmitri N. Zakharov, Jorge Anibal Boscoboinik, Guofeng Wang, and Guangwen Zhou

Sci. Adv. 9 (44), eadh5565. DOI: 10.1126/sciadv.adh5565

View the article online

https://www.science.org/doi/10.1126/sciadv.adh5565

**Permissions** 

https://www.science.org/help/reprints-and-permissions

Use of this article is subject to the Terms of service